

Article

Predicting the Level of Background Current Noise in Graphene Biosensor through a Non-Covalent Functionalization Process

Chao-yi Zhu ^{1,2}, Zi-hong Lin ³, Da-yong Zhang ¹, Jing-yuan Shi ¹, Song-ang Peng ^{1,4,*} and Zhi Jin ^{1,*}

¹ High-Frequency High-Voltage Device and Integrated Circuits R&D Center, Institute of Microelectronics of the Chinese Academy of Sciences, Beijing 100029, China

² University of Chinese Academy of Sciences, Beijing 101408, China

³ Coyote Bioscience Co., Ltd., Beijing 100095, China

⁴ Laboratory of Microelectronics Devices and Integrated Technology, Institute of Microelectronics of the Chinese Academy of Sciences, Beijing 100029, China

* Correspondence: pengsongang@ime.ac.cn (S.-a.P.); jinzhi@ime.ac.cn (Z.J.)

Abstract: The rapid worldwide spread of the severe acute respiratory syndrome coronavirus 2 (SARS-CoV-2) has created a series of problems. Detection platforms based on graphene field-effect transistors (GFETs) have been proposed to achieve a rapid diagnosis of SARS-CoV-2 antigen or antibody. For GFET-based biosensors, the graphene surface usually needs to be functionalized to immobilize the bioreceptor and the non-covalent approach is preferred for functionalization because it is believed not to significantly alter the electronic properties of graphene. However, in this work, the non-covalent functionalization introduced by 1-pyrenebutyric acid N-hydroxysuccinimide ester (PBASE) was determined to lead to different changes in electrical properties in graphene samples with different defect densities. The fabricated graphene biosensor can successfully detect SARS-CoV-2 antigen with a concentration as low as 0.91 pg/mL. Further, by careful comparison, we determined that, for GFET fabricated on graphene with a higher defect density, the current variation caused by PBASE modification is greater and the background current noise in the subsequent antigen detection is also larger. Based on this relationship, we can predict the background current noise of the biosensors by evaluating the current change induced by the modification and screen the devices at an early stage of graphene biosensor fabrication for process optimization.

Keywords: SARS-CoV-2; graphene; biosensor; non-covalent functionalization; background current noise



Citation: Zhu, C.-y.; Lin, Z.-h.; Zhang, D.-y.; Shi, J.-y.; Peng, S.-a.; Jin, Z. Predicting the Level of Background Current Noise in Graphene Biosensor through a Non-Covalent Functionalization Process. *Crystals* **2023**, *13*, 359. <https://doi.org/10.3390/cryst13020359>

Academic Editor: Igor Neri

Received: 2 February 2023

Revised: 14 February 2023

Accepted: 16 February 2023

Published: 19 February 2023



Copyright: © 2023 by the authors. Licensee MDPI, Basel, Switzerland. This article is an open access article distributed under the terms and conditions of the Creative Commons Attribution (CC BY) license (<https://creativecommons.org/licenses/by/4.0/>).

1. Introduction

The worldwide epidemic of coronavirus disease 2019 (COVID-19) has threatened public health and caused economic losses. Bioanalytical diagnostic technologies have played an important role in mitigating the rapid spread of the virus and in the early treatment of patients. The early treatment of COVID-19 is critical, as the causative virus (severe acute respiratory syndrome coronavirus 2, SARS-CoV-2) may cause detrimental effects on respiratory muscle despite the relatively mild symptoms [1]. Among the diagnostic techniques currently available, reverse transcription–polymerase chain reaction (RT-PCR) remains the gold standard for the diagnosis of COVID-19 [2]. RT-PCR technology requires many complex steps, such as the isolation of RNA, reverse transcription, polymerase chain reaction, and amplification product detection [3]. These complex processes will undoubtedly increase operating costs and trained professionals are necessary for this technology. There are other limitations to this technology. RT-PCR requires considerable turnaround times considering the multiple stages of sample transport, analysis, and reporting [2]. In addition, this method is susceptible to false negatives and it should be used in combination with other diagnostic reports such as computed tomography (CT) X-ray scan of the

chest [4]. Therefore, other convenient, rapid, and highly sensitive diagnostic techniques are especially desirable.

Since the successful experimental realization of graphene sheets in 2004 [5], the fascinating properties of graphene have attracted extensive interest. Graphene devices with superior room temperature mobility of up to $140,000 \text{ cm}^2/\text{V s}$ have been reported [6]. When considering high-field transport, graphene also has an advantage over conventional semiconductors due to its higher maximum carrier velocity [7]. In addition to the above advantages, graphene is particularly suitable for sensor applications because its electronic properties are very sensitive to changes in the external environment. For example, graphene exhibits a highly sensitive electrical response to molecules adsorbed on its surface [8]. This sensitivity stems from the two-dimensional nature of graphene (i.e., every atom in graphene can be exposed to the adsorbed molecules) [9]. This property allows graphene to have the largest sensing area per unit volume. A typical example of the ultra-high sensitivity of graphene-based sensors is the gas sensor that can detect the adsorption of individual gas molecules [10]. There have been tremendous efforts in applying graphene to novel sensors for COVID-19 tests. A recent study shows that adding graphene films to the structure of a surface plasmon resonance (SPR) biosensor can effectively improve the sensitivity of the biosensor [11]. The proposed SPR biosensor can detect the SARS-CoV-2 antibodies at the nM level. The field effect is also a very reliable sensing mechanism [12], and this effect has led to the creation and mass application of graphene field-effect transistor (GFET)-based biosensors. In GFET-based biosensors, the gate voltage can be applied to the graphene channel through a solid dielectric layer or an electrolyte solution to change the electric field distribution on the graphene surface, corresponding to the back-gated GFET (BGFET) and the solution-gated GFET (SGFET) configuration, respectively. GFET-based biosensors have enabled the detection of many biomarkers, such as DNA molecules [13], bovine serum albumin (BSA) [14], and Immunoglobulin E (IgE) protein [15]. Functionalization of channel surfaces in GFETs using SARS-CoV-2 spike antibody can provide biosensors with the ability to detect viral antigen protein and SARS-CoV-2 virus from clinical samples [16]. More importantly, this GFET-based biosensor can effectively discriminate between the antigen protein of SARS-CoV-2 and that of the Middle East respiratory syndrome coronavirus (MERS-CoV) [16]. In 2021, a GFET-based biosensor for ultrasensitive detection of the viral antibody of SARS-CoV-2 has been developed [17], and the reported limit of detection (LoD) for monitoring antibody has been reduced to an extremely low value (2.6 aM). Compared to the antibody detection at the nM concentration level achieved in the SPR biosensor, the GFET-based biosensor has a higher sensitivity. Although GFET-based biosensors are a promising diagnostic technology, the surface of graphene itself is intrinsically chemically inert due to the absence of dangling bonds [18]. Therefore, graphene surfaces often need to be functionalized for subsequently selective detection of biomarkers. In the step of functionalization of graphene surface, both covalent [19] and non-covalent [20] methods can be used. In general knowledge, non-covalent functionalization via π -interactions can attach functional groups to the graphene surface without disturbing electronic network [21]. However, the detailed evaluation and the comprehensive investigation of the effects of non-covalent functionalization on the properties of graphene are still lacking. On the other hand, for graphene biosensors, the background current noise is an important device metric. This is because the LoD of biosensors is proportional to the average noise level (i.e., the lower the noise level, the lower the LoD) [17]. Therefore, many efforts have been made to reduce noise in GFET-based biosensors, such as sensing through the changes in the intensity of the alternating current (AC) signal [22] and using peptide nucleic acid (PNA, an electrically neutral molecule) as a probe for detection [23]. In addition to noise reduction, for high-volume fabrication of graphene-based biosensors, a method that can evaluate the noise performance of the final device during the fabrication process (without the device being fully fabricated) is also essential for timely optimization of the fabrication process to reduce costs. However, such a method is still lacking. According to a recent study [24], a higher noise corresponds to a greater level of defectiveness in the material. Therefore,

timely monitoring of defect levels in graphene materials during fabrication can also help to assess noise in the final biosensors. In 2022, a graphene defect detection technique based on advanced algorithm and electrical impedance tomography was reported [25]. However, the evaluation of noise in graphene device was not reported in this study.

In this work, we fabricated SGFET devices as the detection platform for the SARS-CoV-2 antigen protein and proposed a method to estimate the noise in the final biosensors without completely fabricating the devices. The graphene devices were carefully fabricated and the non-covalent functionalization of graphene surfaces was performed using 1-pyrenebutyric acid N-hydroxysuccinimide ester (PBASE). PBASE is a heterobifunctional linker molecule that can adsorb to the graphene surfaces through π - π interactions (via a pyrene group) and it also provides a standard N-hydroxysuccinimide (NHS) ester ligand that can covalently immobilize SARS-CoV-2 antibody molecules [26]. Our SGFET-based biosensor successfully detected SARS-CoV-2 antigen protein in phosphate-buffered saline (PBS) at a concentration as low as 0.91 pg/mL. Multiple characterization tools were used to monitor graphene devices in various steps of biosensing. Raman spectroscopy was used to characterize the defect densities in different regions on graphene grown by chemical vapor deposition (CVD). We fabricated SGFET devices on regions with different defect densities. By this approach, we reported a detailed evaluation and comprehensive study of the influences of non-covalent functionalization on graphene with different defect levels. Although it is generally perceived that the non-covalent functionalization does not significantly change the electronic properties of graphene, the results of the transport measurements in this work indicate that several graphene transistors prepared on graphene with different defect levels (with the same device configuration) produce different responses to the adsorption of PBASE molecules. More importantly, in subsequent measurements of the real-time response of the biosensors toward SARS-CoV-2 antigen protein, the device that is more affected during the non-covalent functionalization (i.e., the channel current (I_{DS}) of the device decreases more dramatically after non-covalent functionalization) exhibits greater background current noise. A recent study has shown that defects in graphene can enhance the adsorption of molecules [27]. Therefore, the greater variation in I_{DS} of the device prepared on graphene with higher defect level after the PBASE modification can be attributed to the enhanced adsorption of PBASE due to the defects in graphene. The higher defect level in graphene can also cause the greater noise. Our work first uses the variation in I_{DS} caused by the PBASE functionalization to reflect the macroscopic level of defects in graphene, allowing the background current noise level in the final biosensors to be predicted by convenient electrical measurements in the fabrication process. According to our study, the level of background current noise of the final fabricated biosensor can be predicted by observing the change in I_{DS} before and after the non-covalent functionalization process introduced by PBASE. Therefore, we can screen devices with better sensing performance (i.e., remove the devices with large current changes after non-covalent functionalization) at an early stage of graphene-based biosensor fabrication based on the experimental observations.

2. Experiment

2.1. SGFET Biosensor Fabrication

First, a 300 nm thick SiO₂ dielectric layer was deposited on the silicon wafer using plasma-enhanced chemical vapor deposition (PECVD). Then, a standard ultraviolet (UV) photolithography process was employed to define the coplanar gate electrodes and external lead electrodes of sensor devices. During this process, a layer of photoresist (AZ5214) was spin-coated onto the surface of SiO₂/Si substrate, at 4000 rpm for 1 min, followed by 100 °C baking for 90 sec. After photolithography and development, 3 nm Ti/10 nm Au/10 nm Pt were deposited by electron beam evaporation then the electrodes were manufactured by lift-off. Then, a 100 nm thick Si₃N₄ layer was deposited by PECVD to passivate a large portion of the external leads. After that, the photolithography process was used again to define the etching window which exposes the gate electrode, some of the external leads, and the

SiO₂ substrate. Inductively coupled plasma (ICP) etching was employed to etch away the Si₃N₄ dielectric inside the window. Graphene films were grown via the CVD method [28]. Then, the grown graphene films were transferred to the etched substrate via the reported poly (methyl methacrylate) (PMMA)-assisted transfer approach [29]. Annealing treatment at 250 °C under N₂ atmosphere was used to enhance the conformity between graphene and the substrate. The transferred graphene was patterned by combining electron beam lithography and O₂-plasma etching. The final step in the graphene-based biosensor device fabrication process is the deposition of the source and drain electrodes connecting the graphene channel to the exposed external leads. The source and drain electrodes of 3 nm Al/2 nm Ti/10 nm Au/5 nm Pt were prepared by the combination of electron beam lithography, electron beam evaporation, and lift-off process.

2.2. Functionalization of Graphene

First, the entire graphene biosensor chip was immersed into the methanol solution of PBASE (Shanghai Aladdin Biochemical Technology Co., Ltd., Shanghai, China) at 5 mM for 2 h at room temperature. Then, the chip was fished out of the PBASE solution and gently rinsed several times with PBS and deionized water. Subsequently, the functionalized biosensor device was soaked in 0.5 mg/mL SARS-CoV-2 antibody (SARS-CoV-2 antibody and antigen were obtained from Coyote Bioscience Co., Ltd., Beijing, China) solution for 2 h. In the end, the graphene device was gently rinsed with PBS to remove the SARS-CoV-2 antibodies not immobilized on the graphene surface.

2.3. Experimental Characterization

The morphology and quality of graphene films before and after the PBASE functionalization were characterized by Raman spectroscopy, atomic force microscope (AFM) park system, and scanning electron microscope (SEM, Hitachi S4800, acceleration voltage 3.0 kV). The Raman spectra were acquired with a LabRAM HR Evolution Raman Spectrometer (HORIBA Jobin Yvon) equipped with a 532 nm wavelength laser. The graphene surface morphology after antigen detection was measured by AFM and SEM. The electrical performance of biosensors was captured with a Keysight B1500A semiconductor device analyzer and a probe station. In the extraction of device transfer curves, the drain-source voltage (V_{DS}) was fixed to 100 mV, and the gate voltage (V_{TG}) was swept from -0.5 to 0.5 V. The sweep rate of V_{TG} was 20 mV/s. During the time-resolved detection of SARS-CoV-2 antigen proteins, the V_{DS} was fixed to 100 mV and the V_{TG} was fixed to 200 mV. The SARS-CoV-2 antigen protein solutions of different concentrations were prepared by serial dilutions of the stock solution of the antigen protein.

3. Results and Discussion

Figure 1 presents a three-dimensional (3D) schematic of the graphene-based biosensor device fabricated in this work, an optical photograph of the biosensor device wafer, and a micrograph of two biosensor devices. From the 3D schematic in Figure 1a, the PBASE molecules were adsorbed onto the graphene channel surface through π - π interactions to achieve non-covalent functionalization. Subsequently, the SARS-CoV-2 antibody was immobilized onto the graphene surface through PBASE [16] to enable a SARS-CoV-2 antigen protein detection platform. After the detection platform was prepared, the biorecognition of the antigen protein by the immobilized antibody (as shown by the light gray dashed arrow in Figure 1a) would occur when the PBS solution covering the SGFET device contained the antigen protein. This led to a change in the electrical properties of the SGFET device.

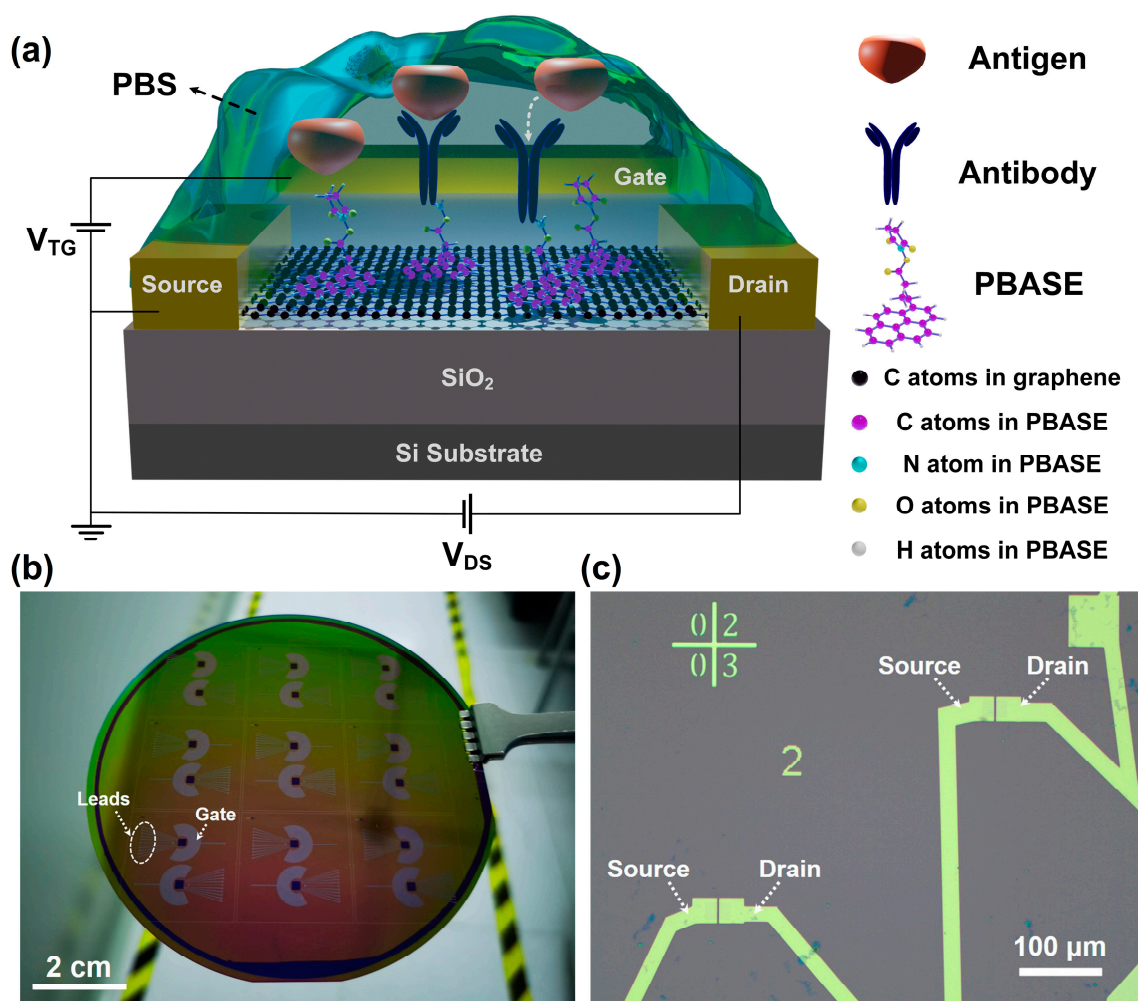


Figure 1. Three-dimensional (3D) schematic, the optical image, and the micrograph of the solution-gated graphene field-effect transistor (SGFET)-based biosensors. (a) The 3D schematic of the SGFET-based biosensor fabricated in this work and the bias configuration in electrical measurements. PBASE, 1-Pyrenebutyric acid N-hydroxysuccinimide ester. PBS, phosphate-buffered saline. V_{TG} : gate voltage. V_{DS} : drain-source voltage. The light gray dashed arrow indicates the biorecognition event of the antigen protein by the immobilized antibody. (b) The optical image of biosensor devices fabricated in bulk on a 100 mm wafer. The lavender half-ring indicated by the “Gate” mark is the in-plane gate electrode. Several thin lavender strips indicated by “Leads” are the external leads of the device. (c) The micrograph of two SGFET-based biosensors. Inside the slit between the source and drain electrodes is a graphene channel exposed to the electrolyte solution. The length of the exposed channel is 2 μm .

During the electrical measurements (the bias configuration is shown in Figure 1a), the application of the V_{TG} leads to the formation of two electrical double layers (EDLs) at the gate electrode/electrolyte solution and the graphene channel/electrolyte solution interfaces, which can be regarded as insulating layers [30]. Thus, these EDLs can be described in terms of parallel plate capacitors with a geometrical capacitance per unit area $C_{EDL} = \epsilon_r \epsilon_0 / \lambda_D$, where ϵ_r is the relative permittivity of electrolyte, ϵ_0 is the vacuum permittivity, and λ_D is the Debye length [31]. For the graphene channel/electrolyte solution interface, in addition to the interfacial capacitance derived from the EDL, the contribution of quantum capacitance (C_Q) should also be considered [32]. The total capacitance of the graphene channel/electrolyte solution interface includes both the capacitance of the EDL and the C_Q of graphene itself. Therefore, the total gate capacitance of the SGFET biosensor is composed of a series connection of the capacitance of the two EDLs at the gate

electrode/electrolyte solution and the graphene channel/electrolyte solution interfaces and the quantum capacitance of the graphene [33]. In the conventional structure of SGFET devices, a large gate electrode out of plane is often required, such as an Ag/AgCl reference electrode [14] or a metallic wire made of Pt [30]. This out-of-plane gate electrode increases the difficulty of the operation and the complexity of the measurement setup. An alternative architecture for SGFET, in which the source, drain, and gate electrodes are in the same plane, has been reported [34]. In this device structure, an in-plane metallic gate electrode replaces the conventional metallic wire and this in-plane metallic gate electrode provides an efficient transistor gate-controlling. Therefore, we also adopted this integrated device configuration including in-plane gate electrodes (as shown in Figure 1a,b) to fabricate SGFET biosensor devices at scale on a 100 mm wafer (as depicted in Figure 1b). Furthermore, considering that the capacitance of EDL is proportional to the contact area of the interface, the area of the in-plane gate electrode/electrolyte solution interface (S_{gate}) of the device in this work is much larger than the area of the graphene channel/electrolyte solution interface ($S_{graphene}$) ($S_{gate}/S_{graphene} > 10^4$, as shown in Figure 1b,c). This design is employed to reduce the effect of the capacitance of the gate electrode/electrolyte solution interface. Hence, during the operation of SGFET devices, the total gate capacitance only needs to include the contributions of the capacitance of the EDL at the graphene channel/electrolyte solution interface and the quantum capacitance of graphene, as demonstrated in the previous literature [31].

As the first step in the functionalization of SGFET-based biosensors, the non-covalent functionalization introduced by PBASE molecules needs to be carefully characterized and systematically studied. Raman spectroscopy is a powerful non-destructive characterization tool for carbon materials, and it allows the evaluation of doping in graphene [35]. In the Raman spectrum of graphene, the prominent Raman features are G peak and 2D peak. The G peak is attributed to the doubly degenerate zone center E_{2g} mode [36], and the 2D peak involves phonons at the $\mathbf{K} + \Delta\mathbf{k}$ points in the Brillouin zone [37]. From the Raman spectra in Figure 2, the position of G peak (ω_G) is 1578.895 cm^{-1} and the position of 2D peak (ω_{2D}) is 2664.844 cm^{-1} before the PBASE molecules modified the graphene surface. However, after the non-covalent functionalization induced by PBASE, the ω_G shifts to 1581.337 cm^{-1} and the ω_{2D} shifts to 2666.086 cm^{-1} . The non-covalent functionalization of PBASE induces blueshifts in both G and 2D peaks, meanwhile the shift of G peak (2.442 cm^{-1}) is larger than that of 2D peak (1.242 cm^{-1}), suggesting that the blueshifts of the Raman peaks might be due to the hole doping of graphene [37]. The hole-doping effect of PBASE can be attributed to its electron-withdrawing property [38].

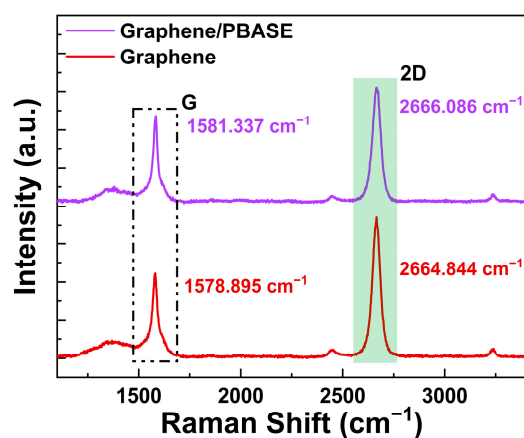


Figure 2. The Raman spectra of graphene film before and after the non-covalent functionalization of graphene surface using PBASE molecules.

AFM is also commonly used as a valuable tool to characterize the surface morphology of the graphene sheet before and after the PBASE modification [16]. Figure 3 shows

the changes in the surface morphology of graphene film before and after the PBASE modification and the corresponding height profiles and histograms. The AFM images of graphene film before and after PBASE modification are shown in Figures 3a and 3b, respectively. The root mean square (RMS) surface roughness of graphene is extracted from an area of $2.5 \times 2.5 \mu\text{m}^2$ (within the white dashed box in the AFM images in Figure 3a,b). Before the adsorption of PBASE molecules onto the surface of graphene, the RMS roughness of graphene is $\sim 2.356 \text{ nm}$ and that of the SiO_2 substrate is $\sim 2.168 \text{ nm}$. The relatively high surface roughness of graphene and SiO_2 substrate is due to some over-etching of the underlying SiO_2 substrate during the ICP etching of the Si_3N_4 dielectric.

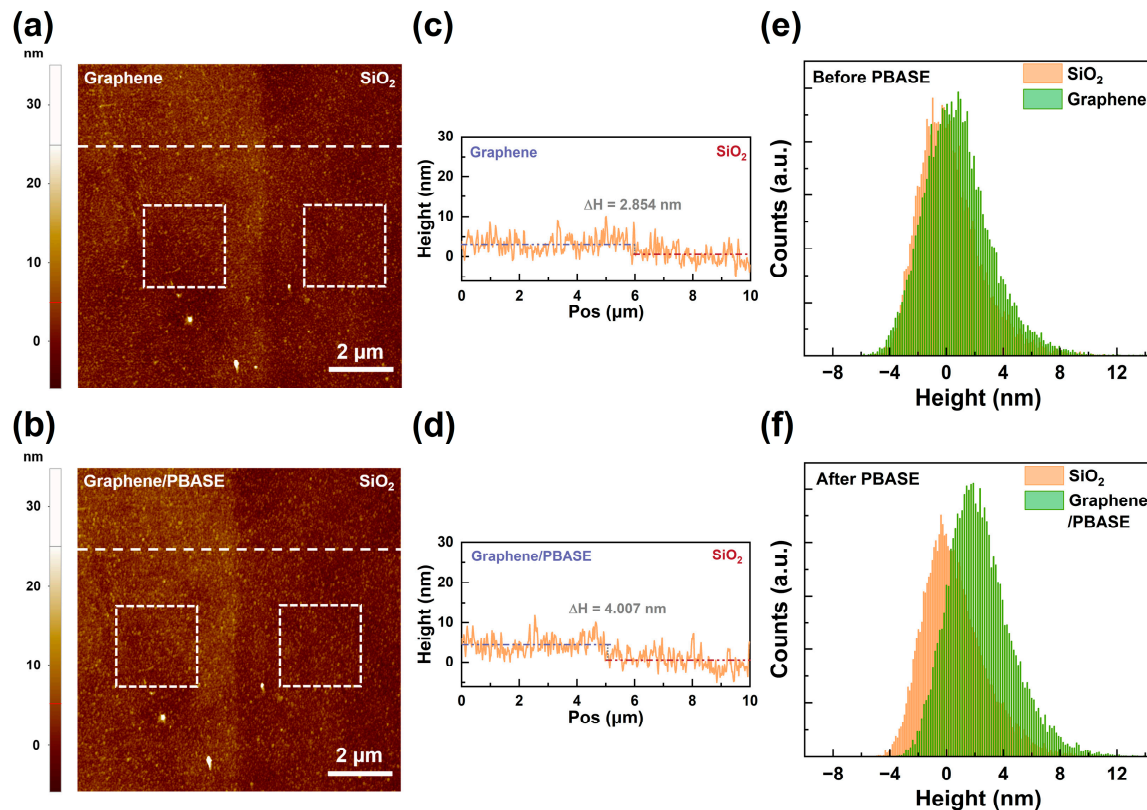


Figure 3. Atomic force microscope (AFM) characterization of graphene morphology before and after the non-covalent functionalization induced by PBASE, and the corresponding height profiles and histograms. (a,b): The AFM images of the graphene sheet and SiO_2 substrate before and after the adsorption of PBASE molecules, respectively. (c,d): The height profiles along the white dashed lines in (a) and (b), respectively. (e,f): The histograms of the height of graphene and SiO_2 substrate before and after the PBASE modification, respectively. The histograms are extracted from the white dashed boxes in (a) and (b), respectively. The area of each box is $2.5 \times 2.5 \mu\text{m}^2$.

After the PBASE adsorption, the RMS roughness of graphene is $\sim 2.304 \text{ nm}$ and that of the SiO_2 substrate is $\sim 2.179 \text{ nm}$. The surface roughness of the SiO_2 substrate does not change much before and after the modification. However, there is a slight decrease in the surface roughness of the graphene film after the adsorption of PBASE. The self-assembly of PBASE molecules on the graphene surface was reported to planarize the defective graphene surface due to the strong $\pi - \pi$ stacking [39]. This is probably the reason for the slight reduction in graphene surface roughness after the adsorption of PBASE. As shown in the corresponding height profiles before and after non-covalent functionalization (Figure 3c,d), the height of the PBASE self-assembled molecules (SAM) layer is $\sim 1.153 \text{ nm}$. This value is similar to the height value of the PBASE SAM layer reported in other literature [39]. In addition, before PBASE adsorption, the height histogram of graphene almost overlaps with that of the SiO_2 substrate (Figure 3e). However, after

the PBASE modification of the graphene surface, the height histogram of the graphene sheet is significantly separated from that of the SiO₂ substrate, and the overall height of the graphene is clearly larger than that of the SiO₂ substrate (Figure 3f). The SEM images in Figure S1 (see Supplementary Materials) also illustrate the successful PBASE adsorption. Before the PBASE functionalization, the surface of the graphene channel was clean (Figure S1a). However, after PBASE modification, several bright spots appeared on the originally clean graphene surface (marked by the arrows in Figure S1b). The characterization results of AFM and SEM adequately demonstrate the successful non-covalent functionalization of graphene via PBASE molecules.

To demonstrate that the prepared SGFET biosensors can effectively capture the SARS-CoV-2 antigen proteins, the graphene channel morphology of the SGFET device after monitoring the time-resolved current response to antigen protein was characterized by AFM. As can be seen from the AFM image in Figure 4a, many high spots appear on the surface of the graphene channel after the antigen detection, indicating that the antigen proteins are adsorbed onto the graphene surface. In addition, the RMS roughness of the graphene sheet after antigen detection increases to ~ 4.254 nm, while there is a smaller increment in the RMS roughness of the SiO₂ substrate (from ~ 2.179 nm to ~ 2.914 nm, compared to the roughness of SiO₂ in the AFM image after PBASE modification). From the corresponding height profiles (Figure 4b), the height of the graphene film after antigen detection increases by ~ 5.247 nm. Compared with the height histograms after PBASE adsorption (Figure 3f), the separation between the height histogram of the graphene sheet and that of the SiO₂ substrate is further increased after antigen detection (Figure 4c). The SEM image also confirms the adsorption of the antigen on the graphene surface after the detection. As shown in Figure S1c, a larger bright spot (marked by an arrow) appeared on the graphene surface after the detection of antigen protein. This indicates the adsorption of the antigen on the graphene surface.

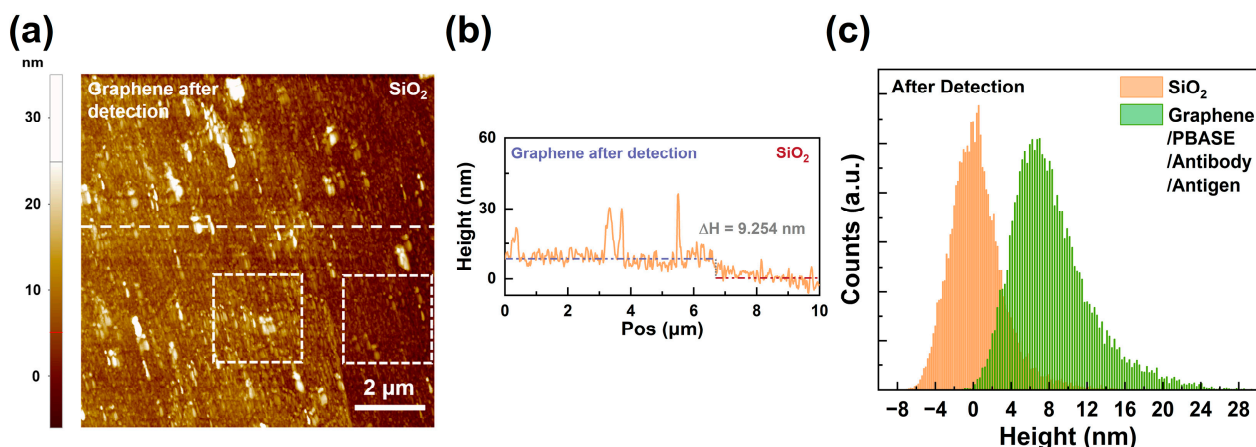


Figure 4. AFM characterization of graphene morphology after the detection of SARS-CoV-2 antigen protein, and the corresponding height profile and histograms. (a) The AFM image of graphene film and SiO₂ substrate after the antigen detection. (b) The height profile along the white dashed line in (a). (c) The histograms of the height of graphene and SiO₂ substrate after the antigen detection. The histograms are extracted from the white dashed boxes in (a) and the area of each box is $2.5 \times 2.5 \mu\text{m}^2$.

To accurately evaluate the device performance of the SGFET biosensors, we monitored the channel currents of several graphene transistors at different functionalization steps and after the real-time detection of antigen proteins. The results of electrical characterization are depicted in Figure 5. Throughout the electrical measurements, 1 mM PBS solution was selected as the electrolyte solution covering the in-plane gate electrode and the exposed graphene channel to provide effective solution-gating. In this study, the graphene films grown by CVD have different defect levels in different regions. Raman spectroscopy was employed to confirm the defect density in different regions of graphene. The D peak related

to defects [40] (at $\sim 1350\text{ cm}^{-1}$) was always observed in different regions and the D to G peak intensity ratios $I(D)/I(G)$ were different in various regions (Figure S2). Three representative graphene regions were labeled as “Region 1”, “Region 2”, and “Region 3”. The $I(D)/I(G)$ values corresponding to the three regions were extracted by fitting peaks with the Lorentzian function [41] (Figure S2b–d). The corresponding $I(D)/I(G)$ values for Region 1, Region 2, and Region 3 are 0.191, 0.193, and 0.204, respectively. The $I(D)/I(G)$ increases as the defect density increases, and this ratio reaches its maximum value when two defects are closer than the average distance an electron–hole pair travels before scattering with a phonon [42]. In all regions, the intensity of G peak remains lower than that of 2D peak (Figure S2a), indicating that the $I(D)/I(G)$ has not reached its top and the defect density is still small [41,42]. Therefore, the density of defects is higher in the region with higher $I(D)/I(G)$ value. Three SGFET biosensor devices were fabricated in Region 1, Region 2, and Region 3, and labeled as “Device 1”, “Device 2”, and “Device 3”, respectively. Thus, the graphene channel in Device 1 has the lowest defect density and that in Device 3 has the highest defect density. These devices have the same device architecture (channel lengths (L_g) are both $2\ \mu\text{m}$ and channel widths are both $20\ \mu\text{m}$). In addition, the drain-source voltage (V_{DS}) of SGFET was kept at $100\ \text{mV}$ during the measurement to avoid possible chemical reactions on the graphene surface [43]. The stability of the fabricated sensor is assessed by repeated electrical characterization of the device. The results of the characterization are shown in Figure S3. An interval of 12 h separated the two repeated electrical characterizations. The device transfer curves obtained from the two measurements almost overlap, which illustrates the stability of our prepared devices. The detailed measurement arrangements are as follows: First, electrical measurements were performed on the SGFET devices before modification, and the transfer curves were recorded. At this point, the devices were labeled as “Bare Graphene”. Subsequently, the non-covalent functionalization of the graphene surface introduced by PBASE molecules was performed, and the transfer curves of the graphene devices were measured again after the adsorption. At this point, the devices were labeled as “PBASE”. Next, the graphene sensors were treated with an antibody incubation process to immobilize the antibody onto the graphene surface. After the incubation of the SARS-CoV-2 antibody, the devices were measured again to record the transfer curves. These devices were labeled as “Antibody” at this stage. Finally, the fabricated graphene biosensors were used to perform consecutive SARS-CoV-2 antigen detection for different concentrations of antigen protein solutions (the experimental details and recipes for antigen detection will be described in detail next). After the antigen detection, the transfer curves of the graphene biosensors were measured again. At this time, these devices were labeled as “Antigen”. The transfer curves of the graphene devices for all the above stages are summarized in Figure 5a–c. Interestingly, the effect of PBASE adsorption on drain–source channel current (I_{DS}) of graphene transistors differs very significantly in different devices (even with the same device geometry and functionalization process). In Device 1, the PBASE adsorption has a small effect on the I_{DS} . In Device 2, after PBASE modification, there is a clear reduction in the device current. However, in Device 3, the PBASE-induced non-covalent functionalization causes a substantial reduction in the I_{DS} . The curves for the transconductance (G_m) of these devices as a function of V_{TG} also illustrate a consistent trend (Figure 5d–f). In Device 1, the G_m of graphene transistor is almost the same before and after non-covalent functionalization (except for some tiny differences). For Device 2, a slightly larger difference in the G_m curves of the device before and after the PBASE adsorption than that of Device 1 is observed. For Device 3, the device has significantly different G_m characteristics before and after the PBASE modification of the graphene surface. Considering that the defects enhance the adsorption of molecules on graphene [27,44], the different extent of change in electrical properties after the PBASE adsorption can be attributed to the different defect levels in various devices. In Device 3, the defect density in graphene is the highest and therefore the adsorption of PBASE is the strongest, thus causing the greatest change in the electrical properties.

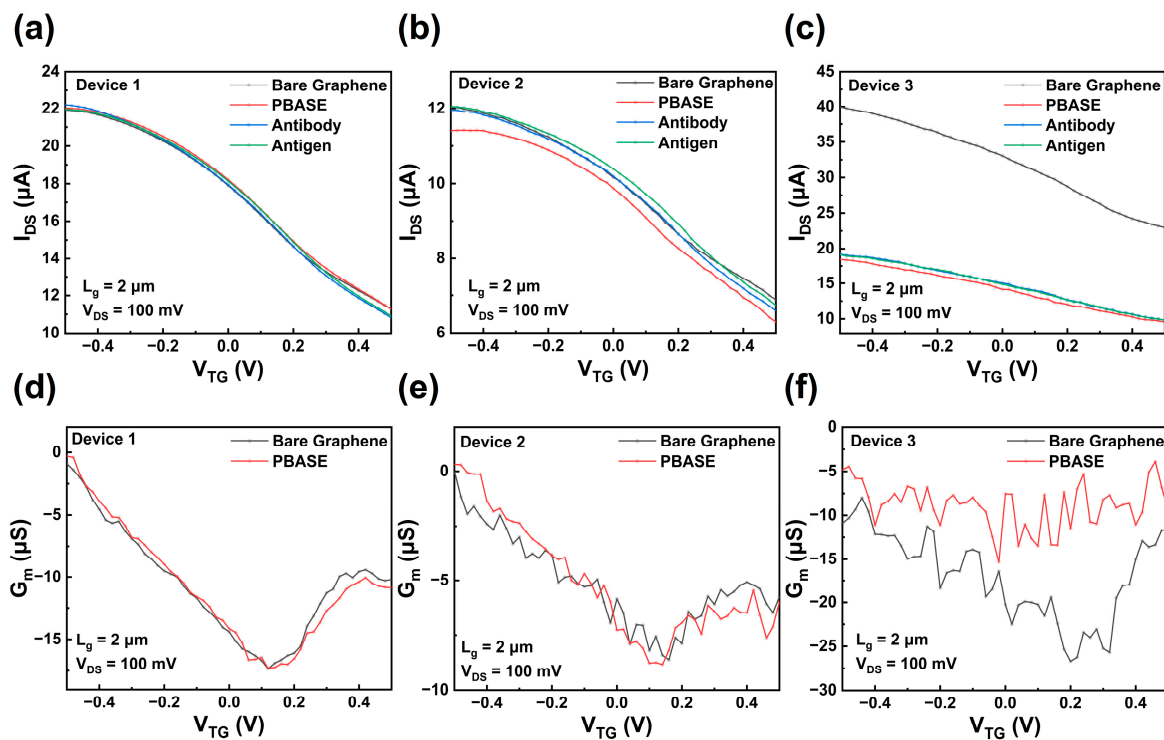


Figure 5. Electrical measurements of prepared SGFET biosensors. (a–c): The transfer curves of three SGFET biosensors labeled as “Device 1”, “Device 2”, and “Device 3”, respectively. I_{DS} : drain–source channel current. (d–f): The transconductance (G_m) curves as a function of V_{TG} for Device 1, Device 2, and Device 3, respectively. The labels “Bare Graphene”, “PBASE”, “Antibody”, and “Antigen” refer to the unmodified graphene device, the graphene device after PBASE adsorption, the graphene device after SARS-CoV-2 antibody immobilization, and the graphene device after SARS-CoV-2 antigen detection, respectively. In all electrical measurements, the V_{DS} of the devices was always maintained at 100 mV. Device 1, Device 2, and Device 3 have the same channel length (L_g , $2 \mu\text{m}$) and channel width ($20 \mu\text{m}$).

A series of consecutive detections of SARS-CoV-2 antigen proteins were performed using the graphene biosensor detection platform developed in this work, and the results are shown in Figure 6. The concentration of the stock solution of SARS-CoV-2 antigen protein is 2 mg/mL . Before conducting the antigen detection, the concentration of the antigen solution was serially diluted from the stock solution to 100 ng/mL , 10 ng/mL , 100 pg/mL , and 10 pg/mL . Before the antigen protein detection, $50 \mu\text{L}$ 1 mM PBS solution was added to the graphene biosensor surface, keeping the solution covering both the in-plane gate electrode and the graphene channel. During the recording of the real-time responses, the V_{TG} was kept at 200 mV . After monitoring the device channel current for a period, 10 pg/mL , 100 pg/mL , 10 ng/mL , and 100 ng/mL antigen solutions were added sequentially to the PBS solution. The volume of each added solution is $5 \mu\text{L}$. The real-time current responses of Device 1, Device 2, and Device 3 toward SARS-CoV-2 antigen proteins are plotted in Figure 6a–c, respectively. For Device 1, a significant current response was detected for the addition of 10 pg/mL antigen solution, while the minimal background current noise was also observed. Considering that the biosensor surface was originally covered with $50 \mu\text{L}$ PBS solution, Device 1 actually succeeded in detecting antigen protein solution with a concentration as low as 0.91 pg/mL ($\frac{10 \text{ pg/mL} \times 5 \mu\text{L}}{55 \mu\text{L}}$). For Device 2, the current response of the biosensor upon the antigen proteins was hardly discernible due to the increased background current noise. The background current noise in Device 3 increases further and the current response of the biosensor toward the antigen proteins becomes more difficult to discriminate. Combined with the changes in electrical properties of the devices before and after the adsorption of PBASE (Figure 5), it seems that the more

the devices are affected by the PBASE modification, the greater the background current noise. Consequently, the more difficult the real-time current response to the antigen is to be discriminated. To quantitatively demonstrate this finding, the change in the I_{DS} of the three devices induced by the PBASE adsorption at $V_{TG} = 200$ mV and $V_{DS} = 100$ mV was calculated, and the background current noise of the three devices while monitoring the real-time response was extracted. The change in I_{DS} is calculated by the following equation:

$$\text{Change in } I_{DS} (\%) = \frac{I_{PBASE} - I_{Bare}}{I_{Bare}}, \quad (1)$$

where I_{PBASE} is the I_{DS} of the PBASE-modified device and I_{Bare} is the I_{DS} of the device without the PBASE modification. The background current noise was estimated from the standard deviation (SD) of the real-time monitoring current of the device for 150 s prior to the addition of the antigen solution, as reported in the previous literature [45]. The relationship between the calculated change in I_{DS} and the background current noise is presented in Figure 6d. It is very clear that the greater the effect of PBASE modification on the I_{DS} of SGFET biosensor, the larger the background current noise of the biosensor in real-time detection. The accuracy of this relationship is confirmed by multiple complementary characterizations (Raman spectroscopy, the measurement of transfer curves, and the monitoring of real-time current responses) that yield consistent regularity. It has been discussed above that the electrical properties of SGFET prepared on graphene region with higher defect density change more after the PBASE modification (due to the enhanced adsorption of PBASE). The proportional relationship between the calculated change in I_{DS} and the $I(D)/I(G)$ is plotted in Figure S4a, indicating that the degree of change in I_{DS} correlates with the level of defect. Furthermore, according to a recent study, a higher noise indicates a higher level of defectiveness in the material [24]. In addition, in graphene grown by CVD, the defects are the dominant source of noise [46]. Thus, the larger background current noise in the fabricated devices can be attributed to the higher defect density in the graphene channel as well, which is confirmed by the relationship between the background current noise and the $I(D)/I(G)$ in Figure S4b. Through the multiple characterization approaches described above (as shown in Figure 6d and Figure S4a,b), it was revealed that the clear physical origin of the relationship between the calculated change in I_{DS} and the background current noise is the level of defect density in the graphene channel. Therefore, based on this clear physical mechanism, the relationship between the calculated change in I_{DS} and the background current noise discovered in this study is accurate. Based on this relationship, if a device has a large change in I_{DS} before and after the PBASE non-covalent functionalization, then we can predict that the device would have a high level of background current noise in real-time detection without performing a subsequent device fabrication process. Excessive background current noise is detrimental to the detection of analytes. Therefore, the relationship between the change in I_{DS} induced by the PBASE modification and the background current noise of the biosensor during the real-time detection discovered in this study is of great significance in biosensor applications. The manufacturing cost of our process for preparing a batch of graphene-based biosensor devices is approximately USD 1000, which includes the cost of experimental consumables, the cost of materials used in the experiments, the cost of using the equipment, and the cost of using the clean environment. Therefore, cost control is a key issue for graphene-based biosensor applications. The relationship discovered in our study facilitates the removal of devices with large current variations due to the non-covalent functionalization, and this screening strategy of SGFET devices through the non-covalent functionalization process can not only reduce the consumption of biological reagents in the subsequent functionalization steps, but also ensure the high performance of the graphene biosensor.

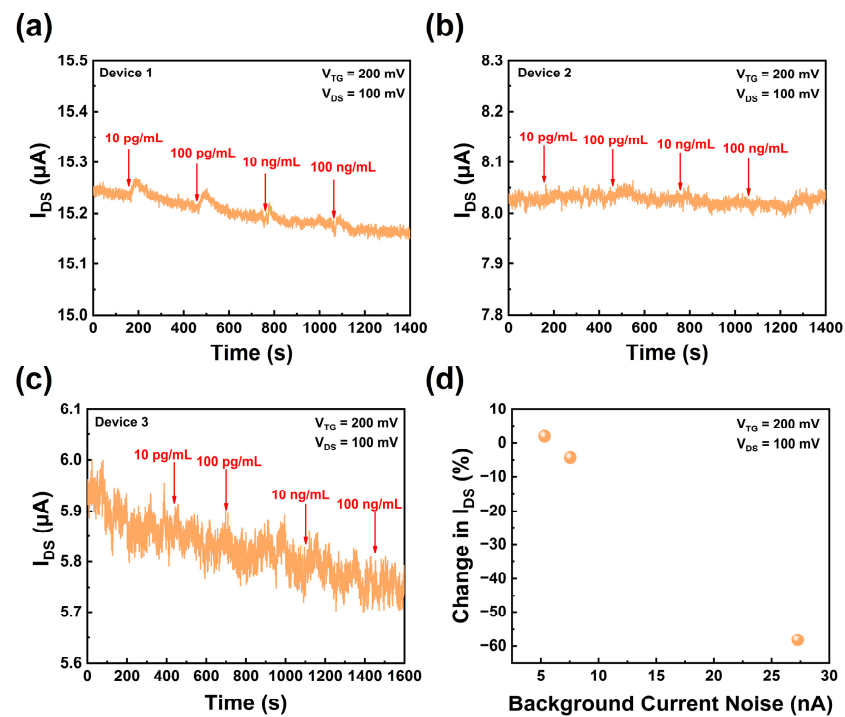


Figure 6. Detection of SARS-CoV-2 antigen protein and the relationship between the change in graphene biosensor current induced by PBASE modification and the background current noise of graphene biosensor. (a–c): The real-time current responses of Device 1, Device 2, and Device 3 upon SARS-CoV-2 antigen proteins, respectively. During the measurements, the V_{TG} was kept at 200 mV and the V_{DS} was kept at 100 mV. (d) The relationship between the calculated change in I_{DS} of the graphene biosensor before and after the non-covalent functionalization of the graphene surface via PBASE and the estimated background current noise of the biosensor during the real-time detection of antigen proteins.

4. Conclusions

In this work, the graphene transistor-based biosensors were fabricated and used as assay platforms to successfully detect the SARS-CoV-2 antigen proteins. The fabricated biosensor can produce a significant current response upon exposure to the antigen solution with a concentration as low as 0.91 pg/mL. Multiple characterization tools were employed to characterize the morphology and quality of graphene film, and the changes in graphene during functionalization were also evaluated. The different levels of defect density in graphene were confirmed by the values of $I(D)/I(G)$ in Raman spectra. For three different graphene regions, the values of $I(D)/I(G)$ are 0.191, 0.193, and 0.204, respectively. Effective adsorption of PBASE molecules and antigen proteins on the graphene surface was confirmed by AFM and SEM characterization. We fabricated graphene biosensors in the three graphene regions with different defect densities. Electrical measurements of graphene biosensors were performed to monitor the electrical properties of the devices during the various steps of functionalization. The real-time current responses of several graphene-based biosensors toward SARS-CoV-2 antigen proteins were also measured. The change in channel current of graphene transistors before and after the PBASE adsorption and the background current noise of the fabricated biosensors were extracted based on the results of electrical characterization and real-time detection. After careful analysis, we determined that in the graphene region with larger defect density, the biosensor has a larger change in channel current after PBASE adsorption and exhibits a higher background current noise in the real-time detection upon antigen proteins, which hinders the observation of the current response. The most dramatic change in I_{DS} observed in electrical measurements after the PBASE adsorption is -58.17% , corresponding to the maximum background current noise of 27.2698 nA. The physical mechanism behind this relationship is that the defects

in graphene both enhance the adsorption of PBASE and contribute to the background current noise in the biosensors. Based on the above relationship discovered in this work, the change in I_{DS} due to PBASE modification can be regarded as an indicator to evaluate the final performance of the biosensor, and we can thus predict the level of background current noise of the fabricated graphene biosensors even before the biosensors are fully prepared. Consequently, a method to screen out the poorly performing devices early in the fabrication of graphene biosensor devices is proposed: first, the current of graphene devices is measured before and after the non-covalent functionalization introduced by PBASE, and then the devices with large current changes are discarded in time. The proposed screening strategy can save the bioreagents required for subsequent functionalization and ensure the performance of the fabricated biosensor.

Supplementary Materials: The following supporting information can be downloaded at: <https://www.mdpi.com/article/10.3390/cryst13020359/s1>, Figure S1: The scanning electron microscopy (SEM) images of (a) the graphene channel before the PBASE functionalization, (b) the graphene channel after the PBASE functionalization, and (c) the graphene channel after antigen detection. The arrows in (b) mark the bright spots due to the PBASE adsorption. The arrow in (c) marks the larger bright spot due to the antigen adsorption; Figure S2: (a) The Raman spectra of chemical vapor deposition-grown graphene in different regions. (b–d): the low-frequency regions in the Raman spectra in three different graphene regions: Region 1, Region 2, and Region 3, respectively; Figure S3: Device transfer curves obtained from two electrical measurements performed on the same fabricated biosensor before the PBASE functionalization. There was an interval of 12 h between the 1st and 2nd measurements; Figure S4: (a) The relationship between the calculated change in the drain–source channel current (I_{DS}) of the graphene biosensor before and after the PBASE functionalization and the D to G peak intensity ratio (I(D)/I(G)) in Raman spectra. (b) The relationship between the estimated background current noise of the biosensor and the I(D)/I(G) in Raman spectra.

Author Contributions: Conceptualization, C.-y.Z., S.-a.P. and Z.J.; validation, C.-y.Z., Z.-h.L., D.-y.Z. and J.-y.S.; formal analysis, Z.-h.L., S.-a.P. and Z.J.; investigation, C.-y.Z.; resources, S.-a.P. and Z.J.; data curation, C.-y.Z.; writing—original draft preparation, C.-y.Z.; writing—review and editing, C.-y.Z., Z.-h.L., S.-a.P. and Z.J.; visualization, C.-y.Z.; supervision, S.-a.P. and Z.J.; project administration, S.-a.P.; funding acquisition, S.-a.P. All authors have read and agreed to the published version of the manuscript.

Funding: STI 2030—Major Projects (2022ZD0209200), Youth Innovation Promotion Association of Chinese Academy of Sciences (2019120), and the opening fund of Key Laboratory of Science and Technology on Silicon Devices, Chinese Academy of Sciences (KLSDTJJ2022-1).

Institutional Review Board Statement: Not applicable.

Informed Consent Statement: Not applicable.

Data Availability Statement: All data that support the findings of this study are included within the article.

Acknowledgments: This work was financially supported by STI 2030—Major Projects (2022ZD0209200), Youth Innovation Promotion Association of Chinese Academy of Sciences (2019120), and the opening fund of Key Laboratory of Science and Technology on Silicon Devices, Chinese Academy of Sciences (KLSDTJJ2022-1). The authors would like to thank Feng-en Chen from the Analysis Center of Tsinghua University for the time of Raman characterization.

Conflicts of Interest: The authors declare no conflict of interest.

References

1. Severin, R.; Franz, C.K.; Farr, E.; Meirelles, C.; Arena, R.; Phillips, S.A.; Bond, S.; Ferraro, F.; Faghy, M. The effects of COVID-19 on respiratory muscle performance: Making the case for respiratory muscle testing and training. *Eur. Respir. Rev.* **2022**, *31*, 220006. [[CrossRef](#)] [[PubMed](#)]
2. Hosseini, A.; Pandey, R.; Osman, E.; Victorious, A.; Li, F.; Didar, T.; Soleymani, L. Roadmap to the Bioanalytical Testing of COVID-19: From Sample Collection to Disease Surveillance. *ACS Sens.* **2020**, *5*, 3328–3345. [[CrossRef](#)]
3. Freeman, W.M.; Walker, S.J.; Vrana, K.E. Quantitative RT-PCR: Pitfalls and potential. *Biotechniques* **1999**, *26*, 112–122. [[CrossRef](#)] [[PubMed](#)]

4. Feng, W.; Newbigging, A.M.; Le, C.; Pang, B.; Peng, H.; Cao, Y.; Wu, J.; Abbas, G.; Song, J.; Wang, D.-B.; et al. Molecular Diagnosis of COVID-19: Challenges and Research Needs. *Anal. Chem.* **2020**, *92*, 10196–10209. [[CrossRef](#)] [[PubMed](#)]
5. Novoselov, K.S.; Geim, A.K.; Morozov, S.V.; Jiang, D.; Zhang, Y.; Dubonos, S.V.; Grigorieva, I.V.; Firsov, A.A. Electric Field Effect in Atomically Thin Carbon Films. *Science* **2004**, *306*, 666–669. [[CrossRef](#)] [[PubMed](#)]
6. Wang, L.; Meric, I.; Huang, P.Y.; Gao, Q.; Gao, Y.; Tran, H.; Taniguchi, T.; Watanabe, K.; Campos, L.M.; Muller, D.A.; et al. One-Dimensional Electrical Contact to a Two-Dimensional Material. *Science* **2013**, *342*, 614–617. [[CrossRef](#)] [[PubMed](#)]
7. Schwierz, F. Graphene transistors. *Nat. Nanotechnol.* **2010**, *5*, 487–496. [[CrossRef](#)]
8. Lin, Y.-M.; Avouris, P. Strong Suppression of Electrical Noise in Bilayer Graphene Nanodevices. *Nano Lett.* **2008**, *8*, 2119–2125. [[CrossRef](#)]
9. Ratnac, K.R.; Yang, W.; Ringer, S.P.; Braet, F. Toward Ubiquitous Environmental Gas Sensors—Capitalizing on the Promise of Graphene. *Environ. Sci. Technol.* **2010**, *44*, 1167–1176. [[CrossRef](#)]
10. Schedin, F.; Geim, A.K.; Morozov, S.V.; Hill, E.W.; Blake, P.; Katsnelson, M.I.; Novoselov, K.S. Detection of individual gas molecules adsorbed on graphene. *Nat. Mater.* **2007**, *6*, 652–655. [[CrossRef](#)]
11. Akib, T.B.; Mou, S.F.; Rahman, M.M.; Rana, M.M.; Islam, M.R.; Mehedi, I.M.; Mahmud, M.A.P.; Kouzani, A.Z. Design and Numerical Analysis of a Graphene-Coated SPR Biosensor for Rapid Detection of the Novel Coronavirus. *Sensors* **2021**, *21*, 3491. [[CrossRef](#)]
12. Fu, W.; Jiang, L.; van Geest, E.P.; Lima, L.M.C.; Schneider, G.F. Sensing at the Surface of Graphene Field-Effect Transistors. *Adv. Mater.* **2017**, *29*, 1603610. [[CrossRef](#)]
13. Lin, C.-T.; Loan, P.T.K.; Chen, T.-Y.; Liu, K.-K.; Chen, C.-H.; Wei, K.-H.; Li, L.-J. Label-Free Electrical Detection of DNA Hybridization on Graphene using Hall Effect Measurements: Revisiting the Sensing Mechanism. *Adv. Funct. Mater.* **2013**, *23*, 2301–2307. [[CrossRef](#)]
14. Ohno, Y.; Maehashi, K.; Yamashiro, Y.; Matsumoto, K. Electrolyte-Gated Graphene Field-Effect Transistors for Detecting pH and Protein Adsorption. *Nano Lett.* **2009**, *9*, 3318–3322. [[CrossRef](#)] [[PubMed](#)]
15. Ohno, Y.; Maehashi, K.; Matsumoto, K. Label-Free Biosensors Based on Aptamer-Modified Graphene Field-Effect Transistors. *J. Am. Chem. Soc.* **2010**, *132*, 18012–18013. [[CrossRef](#)] [[PubMed](#)]
16. Seo, G.; Lee, G.; Kim, M.J.; Baek, S.-H.; Choi, M.; Ku, K.B.; Lee, C.-S.; Jun, S.; Park, D.; Kim, H.G.; et al. Correction to Rapid Detection of COVID-19 Causative Virus (SARS-CoV-2) in Human Nasopharyngeal Swab Specimens Using Field-Effect Transistor-Based Biosensor. *ACS Nano* **2020**, *14*, 12257–12258. [[CrossRef](#)] [[PubMed](#)]
17. Kang, H.; Wang, X.; Guo, M.; Dai, C.; Chen, R.; Yang, L.; Wu, Y.; Ying, T.; Zhu, Z.; Wei, D.; et al. Ultrasensitive Detection of SARS-CoV-2 Antibody by Graphene Field-Effect Transistors. *Nano Lett.* **2021**, *21*, 7897–7904. [[CrossRef](#)]
18. Fu, W.; Nef, C.; Knopfmacher, O.; Tarasov, A.; Weiss, M.; Calame, M.; Schönenberger, C. Graphene Transistors Are Insensitive to pH Changes in Solution. *Nano Lett.* **2011**, *11*, 3597–3600. [[CrossRef](#)]
19. Sinitskii, A.; Dimiev, A.; Corley, D.A.; Fursina, A.A.; Kosynkin, D.V.; Tour, J.M. Kinetics of Diazonium Functionalization of Chemically Converted Graphene Nanoribbons. *ACS Nano* **2010**, *4*, 1949–1954. [[CrossRef](#)] [[PubMed](#)]
20. Katoch, J.; Kim, S.N.; Kuang, Z.; Farmer, B.L.; Naik, R.R.; Tatulian, S.A.; Ishigami, M. Structure of a Peptide Adsorbed on Graphene and Graphite. *Nano Lett.* **2012**, *12*, 2342–2346. [[CrossRef](#)]
21. Georgakilas, V.; Otyepka, M.; Bourlinos, A.B.; Chandra, V.; Kim, N.; Kemp, K.C.; Hobza, P.; Zboril, R.; Kim, K.S. Functionalization of Graphene: Covalent and Non-Covalent Approaches, Derivatives and Applications. *Chem. Rev.* **2012**, *112*, 6156–6214. [[CrossRef](#)] [[PubMed](#)]
22. Xiang, L.; Wang, Z.; Liu, Z.; Weigum, S.E.; Yu, Q.; Chen, M.Y. Inkjet-Printed Flexible Biosensor Based on Graphene Field Effect Transistor. *IEEE Sens. J.* **2016**, *16*, 8359–8364. [[CrossRef](#)]
23. Tian, M.; Qiao, M.; Shen, C.; Meng, F.; Frank, L.A.; Krasitskaya, V.V.; Wang, T.; Zhang, X.; Song, R.; Li, Y.; et al. Highly-sensitive graphene field effect transistor biosensor using PNA and DNA probes for RNA detection. *Appl. Surf. Sci.* **2020**, *527*, 146839. [[CrossRef](#)]
24. Shmidt, N.M.; Usikov, A.S.; Shabunina, E.I.; Nashchekin, A.V.; Gushchina, E.V.; Eliseev, I.A.; Petrov, V.N.; Puzyk, M.V.; Avdeev, O.V.; Klotchenko, S.A.; et al. Investigation of the Morphology and Electrical Properties of Graphene Used in the Development of Biosensors for Detection of Influenza Viruses. *Biosensors* **2022**, *12*, 8. [[CrossRef](#)]
25. Sharma, S.K.; Khambampati, A.K.; Kim, K.Y. Hybrid Particle Swarm Optimization–Gravitational Search Algorithm Based Detection of Graphene Defects With Electrical Impedance Tomography. *IEEE Access* **2022**, *10*, 105744–105757. [[CrossRef](#)]
26. Fernandes, E.; Cabral, P.D.; Campos, R.; Machado, G.; Cerqueira, M.F.; Sousa, C.; Freitas, P.P.; Borme, J.; Petrovykh, D.Y.; Alpuim, P. Functionalization of single-layer graphene for immunoassays. *Appl. Surf. Sci.* **2019**, *480*, 709–716. [[CrossRef](#)]
27. Wang, H.-Y.; Jia, Y.; Hao, Z.-W.; Xiao, J.-X. 1,1-Dimethylhydrazine adsorption on intrinsic, vacancy, and N-doped graphene: A first-principle study. *J. Mol. Model.* **2022**, *28*, 227. [[CrossRef](#)]
28. Zhang, D.; Jin, Z.; Shi, J.; Ma, P.; Peng, S.; Liu, X.; Ye, T. The Anisotropy of Field Effect Mobility of CVD Graphene Grown on Copper Foil. *Small* **2014**, *10*, 1761–1764. [[CrossRef](#)]
29. Zhang, X.-R.; Yao, Y.; Peng, S.-A.; Zhu, C.-Y.; Huang, X.-N.; Yan, Y.-P.; Zhang, D.-Y.; Shi, J.-Y.; Jin, Z. Stable p-type chemical doping of graphene with reduced contact resistance by single-layer perfluorinated polymeric sulfonic acid. *Nanotechnology* **2021**, *32*, 155705. [[CrossRef](#)] [[PubMed](#)]

30. Xu, S.; Zhan, J.; Man, B.; Jiang, S.; Yue, W.; Gao, S.; Guo, C.; Liu, H.; Li, Z.; Wang, J.; et al. Real-time reliable determination of binding kinetics of DNA hybridization using a multi-channel graphene biosensor. *Nat. Commun.* **2017**, *8*, 14902. [[CrossRef](#)]
31. Froehlicher, G.; Berciaud, S. Raman spectroscopy of electrochemically gated graphene transistors: Geometrical capacitance, electron-phonon, electron-electron, and electron-defect scattering. *Phys. Rev. B* **2015**, *91*, 205413. [[CrossRef](#)]
32. Dankerl, M.; Hauf, M.V.; Lippert, A.; Hess, L.H.; Birner, S.; Sharp, I.D.; Mahmood, A.; Mallet, P.; Veuillen, J.-Y.; Stutzmann, M.; et al. Graphene Solution-Gated Field-Effect Transistor Array for Sensing Applications. *Adv. Funct. Mater.* **2010**, *20*, 3117–3124. [[CrossRef](#)]
33. Ye, J.; Craciun, M.F.; Koshino, M.; Russo, S.; Inoue, S.; Yuan, H.; Shimotani, H.; Morpurgo, A.F.; Iwasa, Y. Accessing the transport properties of graphene and its multilayers at high carrier density. *Proc. Natl. Acad. Sci. USA* **2011**, *108*, 13002–13006. [[CrossRef](#)]
34. Vieira, N.C.S.; Borme, J.; Machado, G.; Cerqueira, F.; Freitas, P.P.; Zucolotto, V.; Peres, N.M.R.; Alpuim, P. Graphene field-effect transistor array with integrated electrolytic gates scaled to 200 nm. *J. Phys. Condens. Matter* **2016**, *28*, 085302. [[CrossRef](#)] [[PubMed](#)]
35. Casiraghi, C.; Pisana, S.; Novoselov, K.S.; Geim, A.K.; Ferrari, A.C. Raman fingerprint of charged impurities in graphene. *Appl. Phys. Lett.* **2007**, *91*, 233108. [[CrossRef](#)]
36. Ferrari, A.C.; Meyer, J.C.; Scardaci, V.; Casiraghi, C.; Lazzeri, M.; Mauri, F.; Piscanec, S.; Jiang, D.; Novoselov, K.S.; Roth, S.; et al. Raman Spectrum of Graphene and Graphene Layers. *Phys. Rev. Lett.* **2006**, *97*, 187401. [[CrossRef](#)] [[PubMed](#)]
37. Das, A.; Pisana, S.; Chakraborty, B.; Piscanec, S.; Saha, S.K.; Waghmare, U.V.; Novoselov, K.S.; Krishnamurthy, H.R.; Geim, A.K.; Ferrari, A.C.; et al. Monitoring dopants by Raman scattering in an electrochemically top-gated graphene transistor. *Nat. Nanotechnol.* **2008**, *3*, 210–215. [[CrossRef](#)]
38. Wu, G.; Tang, X.; Meyyappan, M.; Lai, K.W.C. Doping effects of surface functionalization on graphene with aromatic molecule and organic solvents. *Appl. Surf. Sci.* **2017**, *425*, 713–721. [[CrossRef](#)]
39. Liu, Y.; Yuan, L.; Yang, M.; Zheng, Y.; Li, L.; Gao, L.; Nerngchamnon, N.; Nai, C.T.; Sangeeth, C.S.S.; Feng, Y.P.; et al. Giant enhancement in vertical conductivity of stacked CVD graphene sheets by self-assembled molecular layers. *Nat. Commun.* **2014**, *5*, 5461. [[CrossRef](#)] [[PubMed](#)]
40. Malard, L.M.; Pimenta, M.A.; Dresselhaus, G.; Dresselhaus, M.S. Raman spectroscopy in graphene. *Phys. Rep.* **2009**, *473*, 51–87. [[CrossRef](#)]
41. Eckmann, A.; Felten, A.; Mishchenko, A.; Britnell, L.; Krupke, R.; Novoselov, K.S.; Casiraghi, C. Probing the Nature of Defects in Graphene by Raman Spectroscopy. *Nano Lett.* **2012**, *12*, 3925–3930. [[CrossRef](#)] [[PubMed](#)]
42. Cancado, L.G.; Jorio, A.; Ferreira, E.H.M.; Stavale, F.; Achete, C.A.; Capaz, R.B.; Moutinho, M.V.O.; Lombardo, A.; Kulmala, T.S.; Ferrari, A.C. Quantifying Defects in Graphene via Raman Spectroscopy at Different Excitation Energies. *Nano Lett.* **2011**, *11*, 3190–3196. [[CrossRef](#)] [[PubMed](#)]
43. Wu, G.; Dai, Z.; Tang, X.; Lin, Z.; Lo, P.K.; Meyyappan, M.; Lai, K.W.C. Graphene Field-Effect Transistors for the Sensitive and Selective Detection of Escherichia coli Using Pyrene-Tagged DNA Aptamer. *Adv. Healthc. Mater.* **2017**, *6*, 1700736. [[CrossRef](#)]
44. Anithaa, V.S.; Shankar, R.; Vijayakumar, S. DFT-based investigation on adsorption of methane on pristine and defected graphene. *Struct. Chem.* **2017**, *28*, 1935–1952. [[CrossRef](#)]
45. Fu, W.; Feng, L.; Panaitov, G.; Kireev, D.; Mayer, D.; Offenhäusser, A.; Krause, H.-J. Biosensing near the neutrality point of graphene. *Sci. Adv.* **2017**, *3*, e1701247. [[CrossRef](#)] [[PubMed](#)]
46. Kochat, V.; Sahoo, A.; Pal, A.N.; Eashwer, S.; Ramalingam, G.; Sampathkumar, A.; Tero, R.; Viet Thu, T.; Kaushal, S.; Okada, H.; et al. Origin of 1/f noise in graphene produced for large-scale applications in electronics. *IET Circuits Devices Syst.* **2015**, *9*, 52–58. [[CrossRef](#)]

Disclaimer/Publisher’s Note: The statements, opinions and data contained in all publications are solely those of the individual author(s) and contributor(s) and not of MDPI and/or the editor(s). MDPI and/or the editor(s) disclaim responsibility for any injury to people or property resulting from any ideas, methods, instructions or products referred to in the content.